Simulations of ion guiding through a straight macrocapillary: Interpretation of an experiment and comparison with nanocapillaries

N. Stolterfoht
Helmholtz-Zentrum Berlin für Materialien und Energie, D-14109 Berlin, Germany
(Received 14 March 2014; published 9 June 2014)

The transmission of 4.5 keV Ar^{7+} ions through a straight cylindrical macrocapillary is simulated in accordance with the results of a recent experiment. A detailed comparison with the results for nanocapillaries is performed. The theoretical method is based on a code previously developed for a nanocapillary. The ion trajectories are affected by the electric field originating from the charges previously deposited on the capillary wall. The tilt angle of the capillary axis relative to the incident beam was varied within 0°–5°. Both the surface conductivity along the capillary wall and the conductivity into the capillary bulk were treated, providing clear evidence that the bulk conductivity is dominant, involving essentially a linear field dependence. By variation of this conductivity the mechanisms for the major experimental observations were revealed. At low conductivity the fluctuations of the mean ion emission angle are explained by the overloading of temporary charge patches, which are missing at high conductivity. Moreover, it is shown that the capillary guiding power decreases with increasing conductivity, in agreement with the experimental results.

DOI: 10.1103/PhysRevA.89.062706 PACS number(s): 61.85.+p, 34.50.Fa, 32.80.Fb

I. INTRODUCTION

During the past few years capillary guiding of ions through insulating nanocapillaries has received a great deal of attention (see [1], and references therein). The guiding occurs when incident ions deposit charges at the capillary surface, which produce an electric field deflecting the following ions. The essential property of the capillary guiding is a self-organizing process, which governs the charge deposition inside the capillaries [2]. The incident ions produce a predominant charge patch in the entrance region. With increasing deposition of the ions, the charge patch increases until the electrostatic field is large enough to deflect the ions. Then the charge deposition decreases until a balance is reached with the charge depletion by the capillary conductivity. At equilibrium the ions are guided along the capillary axis, maintaining their incident charge state during their passage even when the capillary axis is tilted with respect to the incident beam direction.

The initial exploration of the ion-guiding phenomenon in insulating materials has been performed using multiple capillaries in polyethylene terephthalate (PET) [2–4]. Due to the increasing interest in this field, experimental studies of capillary guiding with different materials have been performed in several laboratories [5–13]. These studies confirmed the capillary guiding for various materials and revealed the most important properties of the guiding mechanisms. Also, guiding of charged particles has been successfully performed with single straight capillaries [14–18], single tapered capillaries [19–22], and between parallel glass plates [23,24]. The work with tapered capillaries was motivated by the aim of producing a microscopic ion beam whose direction may be controlled. Submicron beams are attractive for various applications such as selective damage of individual constituents of biological cells [25].

Theoretical studies have provided detailed information about capillary guiding. In a series of pioneering simulations [26–30], a diffusion model was used, wherein the deposited charges perform a random walk along the surface and inside the bulk of the capillary. A different concept was adopted in recent simulations [31,32] involving a nonlinear (exponential) charge-transport model based on the formalism by Frenkel [33]. This nonlinear approach was motivated by previous experiments which showed that the transmitted ion fraction remains practically constant when the incident ion current is changed by orders of magnitude [8]. These experiments provided evidence that the depletion of the deposited charges strongly increases with the electric field produced in the capillary.

In general, the fraction $f(\psi)$ of transmitted ions at equilibrium decreases exponentially with the square of the tilt angle ψ. The capability of insulating capillaries to guide ions at equilibrium is referred to as the guiding power. It can be accounted for by the characteristic *guiding angle* ψ_c, for which the normalized transmission fraction drops as $f(\psi_c)/f(0) = 1/e$. To date, the guiding angle is accepted as a convenient parameter to quantify the guiding power.

Recently, progress in the field of capillary guiding was achieved in experiments by Gruber *et al.* [18] using a single capillary from borosilicate glass (Duran) [34], in which the capillary conductivity was controlled by heating or freezing the capillary material. Most models describing the charge transport in an insulator (such as that by Frenkel [33]) predict a very strong temperature dependence of both the surface as well as the bulk conductivity. This dependence could be used to vary the conductivities by as much as four orders of magnitude by changing the temperature within the range from −25 to 75 °C [18].

The variation of the capillary conductivity resulted in various effects. For instance, at low conductivity the mean emission angle of the transmitted ions exhibited random-type fluctuations, whereas at higher conductivity the mean emission angle remained essentially constant. A significant decrease of the guiding power with increasing conductivity was observed. Moreover, the guiding power depends on the beam current in contrast to the previous results achieved with nanocapillaries [8]. The experiments were interpreted by theoretical models adopted under the assumption that a microscopic treatment is out of reach [18]. The models were based on simplified

rate equations primarily describing guiding under equilibrium conditions. Estimations of the charge transport provided evidence that the bulk conductivity is dominant in comparison with the surface conductivity.

In this work, simulations of the ion transmission through a straight capillary with the dimensions used by Gruber *et al.* [18] are performed. The simulations are similar to those carried out previously for nanocapillaries by the author [31]. As expected, the present microscopic simulations are too time consuming when performed as in previous work [26,31]. Therefore, a substantial approximation was implemented, i.e., each ion that hits the surface deposits a multitude of ion charges; an approximation similarly adopted by Schweigler *et al.* [30] and Pokhil and Cherdyntsev [24]. The calculations show that the bulk conductivity is dominant, involving primarily a linear field dependence. The formalism reveals that the results remain the same when the beam current is varied instead of the bulk conductivity, in agreement with the experiments. Furthermore, the experimentally observed variations of the mean emission angle and the guiding power are reproduced by the simulations.

II. THEORETICAL METHOD

A. Basic considerations for capillaries

The geometrical properties of the macrocapillary used in the previous experiment [18] are outlined in Fig. 1 and Table I. The macrocapillary was made from borosilicate glass with a wall thickness of $s = 70\ \mu$m while the inner diameter amounts to $d = 160\ \mu$m. The outer capillary wall is covered by a metal layer biased to electrical ground. Moreover, the length of the capillary amounts to $L = 11\,400\ \mu$m.

This length and diameter correspond to an aspect ratio of 70 and an aspect angle of 0.8°. The capillary also defines the coordinate system with the origin in the center of the capillary entrance, the z axis along the capillary center axis, the y axis vertical, and the x axis horizontal. In Table I the corresponding data are compared with typical nanocapillaries used in previous studies [8,35].

In the present work the beam conditions of the previous experiments [18] are adopted using 4.5 keV Ar^{7+} ions with a typical current of 10 fA. As an example, an ion incident at the angle of $\psi = 5°$ has energy perpendicular to the capillary axis (y direction) equal to

$$T_y = T_p \sin^2 \psi, \tag{1}$$

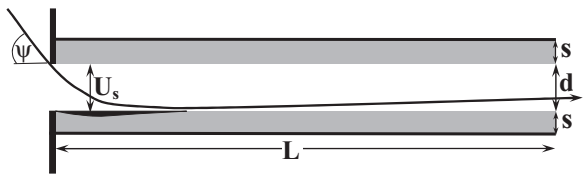

FIG. 1. Schematic drawing of the circular macrocapillary treated in this work. The inner diameter is d, the wall thickness is s, and the capillary length is L. The perpendicular potential difference U_s is required to deflect the 4.5 keV Ar^{7+} ions incident at 5°. The values for the parameters are given in Table I.

TABLE I. Values of the parameters specifying the macrocapillary [18] and nanocapillary [8,35] previously used. The parameters are explained in Fig. 1 and the text.

Parameter	Macrocapillary[a]	Nanocapillary[b]
d (μm)	160	0.2
s (μm)	70	$0.1/\infty$
L (μm)	11 400	30/10
U_s (V)	$\gtrsim$5	$\gtrsim$5
E_y (V/μm)	$\gtrsim$0.06	$\gtrsim$50
Σ_b (S)	3.4×10^{-16}	3.8×10^{-19}
Σ_s (S)	3.1×10^{-18}	3.1×10^{-18}

[a]From [18].
[b]From [35]/[8].

where T_p is the incident energy. To deflect the ions, this perpendicular energy $T_y \approx 35$ eV must be compensated by an effective potential across the capillary diameter (Fig. 1). It is important to note that about the *same* potentials of $U_s \gtrsim 5$ V are required for both the macrocapillary and nanocapillary to ensure the ion deflection to the capillary exit.

On the other hand, the diameters and lengths of the two capillary types differ by about three orders of magnitude (while the aspect ratios are similar). Consequently, all parameters containing a length in the dimension differ significantly. For instance, the field component E_y in the y direction of the nanocapillaries is larger by a factor of ~1000 than that in the present macrocapillary. In fact, the field in the nanocapillary of $\gtrsim$50 V/μm is close to the electric breakthrough value of PET [36] so that nonlinear effects play an important role for the surface conduction [8,31]. In contrast, for the macrocapillary the perpendicular field is only about 0.06 V/μm, which suggests that the field dependence of the charge transport is essentially linear (as in Ohm's law). In this case, the deposited charges are attracted by the grounded metal layer surrounding the capillary wall. Hence, charges deposited at the inner capillary wall are depleted by migration into the capillary bulk.

In Table I two types of nanocapillaries [8,35] are given (separated by a slash) with different locations of the conducting material relevant for the bulk conduction. The nanocapillaries, used by Rajendra-Kumar *et al.* [35], were manufactured with a 0.1-μm-thick wall of highly insulating SiO_2 surrounded by (semi)conducting silicon. This value for s is given in front of the slash in Table I. In this case the bulk conductivities of the nanocapillary and the macrocapillary can be compared directly. To determine the essential differences between the two types of capillaries, rough estimates are performed on the basis that the length parameters can be scaled by about the same factor of 1000.

For the macrocapillary material (Duran) the specific bulk conductivity has been measured at room temperature (22 °C) to be $\sigma_b = 7 \times 10^{-16}$ S/cm [18]. The bulk conductivity is obtained from the well-known formula

$$\Sigma_b = \sigma_b \frac{a_p}{s}, \tag{2}$$

which was estimated by means of the area $a_p \approx x_e l_e$ covered by the entrance patch, where x_e and l_e are its lateral and

longitudinal extensions, respectively. (Realistic dimensions will be given below by the simulations.) Assuming that the specific bulk conductivity does not change significantly, and scaling all length parameters by the same factor 1000, the bulk conductivity of the macrocapillary turns out to be 1000 times larger than that of the nanocapillary (Table I).

On the contrary, similar considerations for the surface conductivity show essentially no change. This is due to the fact that the specific surface conductivity contains no length in its dimension. For Duran it was measured to be $\sigma_s = 10^{-16}$ S [18]. The corresponding surface conductivity is obtained from

$$\Sigma_s = \sigma_s \frac{x_e}{z_p}, \tag{3}$$

where $z_p \approx l_e/2$ is its (mean) distance from the capillary entrance (where a grounded metal layer is located). Again adopting approximate length values scaled by the same factor and assuming no significant change of σ_s, the surface conductivity remains constant. In Table I the results for Σ_b and Σ_s clearly indicate that the bulk conductivity dominates for the macrocapillary, whereas the surface conductivity plays the major role for the nanocapillaries.

In the past, most experiments have been performed with nanocapillaries which had no grounded layer around their walls. Table I shows such an example from previous work [8]. In this case, the bulk migration is less effective [31] as metallized surface layers are further away, located at the front and back sides of the capillary sample (symbolically noted by infinity). With this complex geometry it is difficult to determine the bulk conductivity. However, it can securely be assumed that the bulk conductivity is even lower than the value given in Table I, which suggests a negligible bulk conductivity. On the other hand, the present estimations show that for the macrocapillary the bulk conductivity is dominant. The same conclusion will be drawn within the present simulations.

To determine the charge transport in the macrocapillary with its outer metal layer, it is considered as a capacitor. The charges deposited at the inner capillary surface are screened by the factor $c_s = 2/(\varepsilon_r + 1)$ due to the dielectric material, where ε_r is its relative dielectric constant with $\varepsilon_r = 4.6$ for Duran [34]. The capacity is given by $C = \varepsilon_0 a/s$, where a is the area of the capacitor plates, and s is the wall thickness (mentioned above). Then the decay rate Γ for the deposited charges due to the bulk conductivity Σ_b within the Duran wall is obtained as [30]

$$\Gamma = c_s \frac{\Sigma_b}{C} = c_s \frac{\sigma_b}{\varepsilon_0}, \tag{4}$$

where $\sigma_b = \Sigma_b\, s/a$ is the specific bulk conductivity measured by Gruber *et al.* [18]. It is pointed out that Γ depends neither on the deposited charge nor on the capacitor geometry.

In a linear approach to the charge transport the temporal evolution of the entrance charge patch is given as [2]

$$Q(t) \approx r \frac{J_{\text{in}}}{\Gamma} \left(1 - e^{-\Gamma t}\right), \tag{5}$$

where $r \lesssim 1$ is a reduction factor that accounts for the charge loss due to the current propagated to the capillary exit. The approximate expression (5) allows for an interesting conclusion. The formation of the charge patch is essentially governed by the ratio of the incident beam J_{in} and the decay rate Γ [2]. Indeed, it has been shown experimentally by Gruber *et al.* [18] that the variation of the glass temperature (and hence its conductivity) had the same effect on the guiding properties as the variation of the beam intensity. The same rule holds for the present simulations as will be described in the following.

B. Essentials of the simulations

The simulations were carried out using methods previously developed for nanocapillaries [31,32]. Trajectories of 4.5 keV Ar^{7+} ions were calculated in three dimensions for the cylindrical capillary shown in Fig. 1. The ions were inserted at the tilt angle ψ starting with random x and y values within the circular entrance of the capillary. A divergence of the incident angle of $\pm 0.25^\circ$ was imposed on the incident beam. Figure 1 exhibits a typical trajectory, which is deflected by the electric field produced by the entrance charge patch (shaded in black).

The electric potential within the capillary was evaluated by adding the Coulomb potentials of the individual charges deposited on the capillary surface. As mentioned, the usual calculations applied for nanocapillaries [31,32] are too time consuming for the present case. To drastically reduce the computer time, several thousand ion charges were assumed to be deposited per ion hitting the capillary wall. To ensure that this approximation is feasible, the number of deposited charges was varied using $1000q$, $2000q$, and $5000q$, where q is the ion charge. The charge variation primarily influenced the statistics of the electric potential, whereas the essential properties of the ion guiding remained unchanged.

To judge the feasibility of multiple-charge deposition, it is recalled that the decay rate Γ is independent of the charge so that the size of the charge clusters does not influence their decay. Moreover, the ion trajectories are not much affected by the cluster size, when the mean distance between the clusters is significantly smaller than the capillary diameter. Since the dimensions of the macrocapillary are three orders of magnitude larger than the nanocapillaries, the multiplicity of the clusters may be increased to several thousands. Most of the present results are obtained with $5000q$, which appears to be just below the limit of the cluster approximation.

The grounded metal layer on the outer side of the glass wall affects the field within the capillary. This conducting layer was taken into account by adding images of the deposited charges using the layer as a mirror. In this way, negative image charges were virtually placed outside the capillary, which were added when deducing the electric potential. The major effect of the negative image charges is the potential drop to zero at the metal layer. Also, the mirror charges weakened the potential by roughly 30% within the capillary. The potential was differentiated analytically with respect to the x, y, and z coordinates, yielding the electric-field components E_x, E_y, and E_z, respectively. Then, the trajectories of the 4.5 keV Ar^{7+} ions were evaluated within the capillary by solving Newton's equation of motion.

The ion guiding through the capillary can be maintained only if the deposited charges are reduced by discharge mechanisms [26,31]. For the surface conductivity the deposited

charges are transported along the capillary wall partially to the metal layers covering the capillary front side. However, the main effect of reducing the overcharging of the patches is the charge migration into the bulk of the capillary wall, as pointed out above. Nevertheless, the bulk and surface conductivities are implemented into the calculations.

The charge transport along the surface has been described in detail previously [31,32] so that only a few details are given here. The previous analysis showed that the charge migration is governed by the charge-carrier mobility, which is proportional to the surface conductivity (the proportionality factor is the surface carrier density). The surface charge transport was based on the model by Frenkel [33] which includes both a linear and a nonlinear range, depending on the electric-field strength. A few side calculations for nanocapillaries were performed, extending previous results for the transmission of 3 keV Ne^{7+} ions [32]. Carrier mobilities were used as in the previous work. For the main calculations concerning macrocapillaries, the details of the carrier mobility are not relevant, since in this case the surface charge transport is of minor importance.

The treatment of the dominant bulk conductivity was given above. The discharge occurs with the decay rate Γ, which was determined by Eq. (4) in accordance with the results by Gruber *et al.* [18]. It is again pointed out that Γ is independent of the density of the deposited charge so that the same decay rate applies for all locations within the capillary. As an example, at room temperature of 22 °C, with the values of $\sigma_b = 7.3 \times 10^{-16}$ S/cm [18], $\varepsilon_r = 4.6$, and $\varepsilon_0 = 8.8 \times 10^{-14}$ C/V cm, one obtains a decay rate of $\Gamma \approx 3$ mHz, which corresponds to a mean survival time of 330 s for the deposited charges. Since the decay rate is proportional to the bulk conductivity, it can be changed significantly by varying the capillary temperature [18].

As in the previous simulations [31,32], the ion insertion and the charge transport were treated sequentially in small portions. After a fixed number n_0 of ions (typically $n_0 = 20$) were inserted into the capillary, part of the deposited charges were depleted during a time equal to the insertion time Δt of n_0 ions. This time is given by

$$\Delta t = \frac{q_d\, n_0}{J_{\text{in}}}, \tag{6}$$

where q_d is the deposited charge per incident ion and J_{in} is the corresponding current. To ensure that the sequential treatment is an adequate approximation, the number n_0 was varied in test calculations, showing that the guiding properties did not change within the statistical uncertainties. The incident beam current was $J_{\text{in}} \approx 10$ fA [18] corresponding to $\Delta t = 11$ s with $n_0 = 20$, $q_d = 5000q$, and $q = 7$. These parameters were kept constant throughout the calculations of the present results.

It should be emphasized that in the simulations the bulk discharge is solely governed by the probability of depleting the deposited charges during the interval Δt, which is obtained as

$$p_b = \Gamma\, \Delta t = q_d\, n_0 \frac{\Gamma}{J_{\text{in}}}. \tag{7}$$

With the typical value of $\Gamma = 3$ mHz it follows that $p_b \approx 0.03$, which is sufficiently small to avoid instabilities in the calculations. It is important to note that with constant q_d and n_0, the results of the simulations depend only on the ratio of Γ and J_{in} as already suggested by Eq. (5). In this work, the discharge rate Γ was varied, whereas J_{in} was kept constant. In view of Eq. (7) the same results would be obtained by keeping Γ constant and varying J_{in}. Hence, such variation of J_{in} would be redundant here. The same conditions are valid for the charge transport along the surface, as has already been emphasized for the simulations concerning nanocapillaries [31].

III. RESULTS OF THE SIMULATIONS

A. Trajectories and charge distributions

In the simulations, the tilt angle and the decay rate were varied in accordance with the previous experiments by Gruber *et al.* [18]. First, in view of Fig. 6 in Ref. [18], the calculations were started with the tilt angle of 2°. Two decay rates were chosen corresponding to the cases of a cooled and a heated capillary.

In Fig. 2 ion trajectories and deposited charges are shown for different Q_{in} values ranging from 0.1 to 59 pC. The decay rate for the bulk conductivity was $\Gamma = 0.6$ mHz which corresponds to a cooled capillary. Each Figs. 2(d)–2(f) on the left-hand side shows 20 ion trajectories. In Fig. 2(b) the trajectories appear to be focused in the center of the capillary, which is due to the fact that the repelling field is larger at the bottom than at the top of the capillary. In this case the ions are directly transmitted to the capillary exit. In Figs. 2(c)–2(e) it is seen that the ions follow oscillatory trajectories to the end of the capillary where they leave at varying emission angles. Finally, in Fig. 2(f) the ions are emitted parallel to the capillary axis.

In the right-hand column of Fig. 2 the distributions of deposited charges are shown. In Figs. 2(c)–2(e) on the right-hand side one can distinguish the entrance patch from three additional charge patches. One patch can be seen at the upper wall right after the entrance patch and two more patches are found below near the center of the capillary and at the upper wall near the exit. The charge patches, which are transient and change their position and strength, are responsible for the varying oscillations of the ion trajectories. Finally, in Fig. 2(f) the ion guiding approaches equilibrium, in which the charges are nearly homogeneously distributed all over the capillary wall.

The oscillations of the ion trajectories and the formation of the charge patches observed here for the macrocapillary are very similar to those found for nanocapillaries although their dimensions are much smaller. However, there is an obvious difference. For the nanocapillaries, the entrance charge patch reveals a strong migration of the charges along the wall perpendicular to the capillary axis [31]. In that case, a significant amount of charge is visible in the upper half of the capillary, which is an important effect weakening the perpendicular field E_y near the charge patch. For the present macrocapillary no such charges are visible at the upper wall opposite to the entrance patch, indicating that the perpendicular migration is missing.

This finding provides direct evidence that the surface conductivity is minor for the present macrocapillary, i.e., no field reduction occurs by perpendicular charge migration.

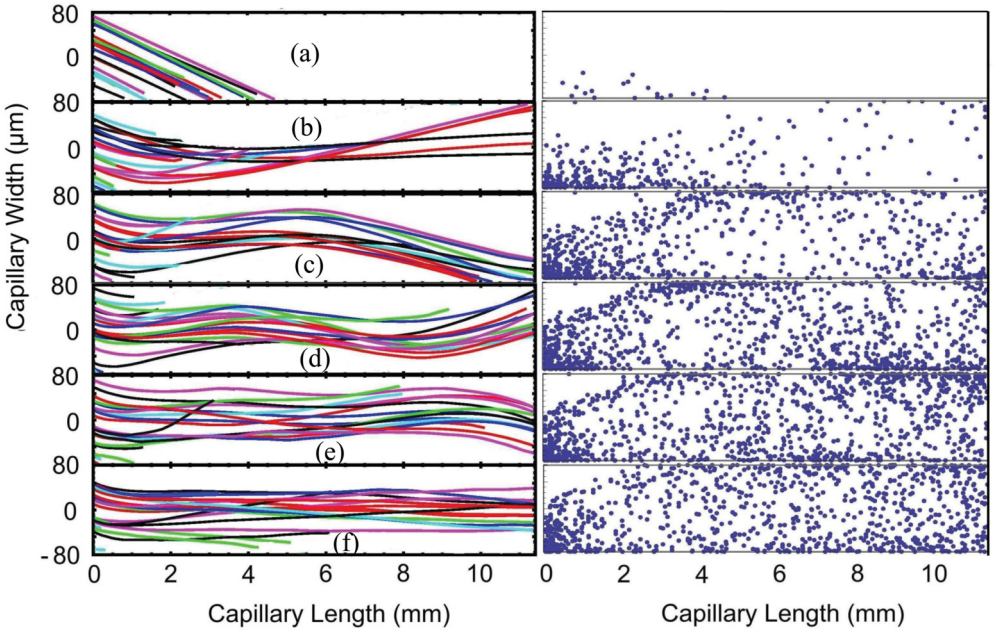

FIG. 2. (Color online) Trajectories of 4.5 keV Ar^{7+} (left-hand panels) and corresponding distributions for the deposited charges (right-hand panels). Each dot corresponds to 5000 ion charges. The titlt angle is 2° and the decay rate due to the bulk conductivity is $\Gamma = 0.6$ mHz. The inserted charge Q_{in} is equal to 0.1 pC in (a), 2.1 pC in (b), 6.8 pC in (c), 15 pC in (d), 29 pC in (e), and 58 pC in (f).

However, the field reduction is an important part of the self-organizing guiding mechanism avoiding the overcharging of the entrance patch. In the case of the macrocapillary the field is reduced only by charge migration into the capillary wall governed by the bulk conductivity. In Fig. 2 the trajectories show that the charge reduction by the bulk conductivity is sufficient to successfully maintain an efficient ion guiding through the capillary.

A further example for ion insertion at the tilt angle of 2° is given in Fig. 3. The bulk conductivity was increased by more than an order of magnitude, reaching a decay rate of 10 mHz. The left-hand side of Figs. 3(b)–3(e) shows that the ion trajectories do not change much with increasing charge insertion. No oscillations of the ion trajectories are observed within the capillary as in the previous figure. The ions are deflected by the entrance charge patch directly to the capillary exit and are emitted essentially under the same

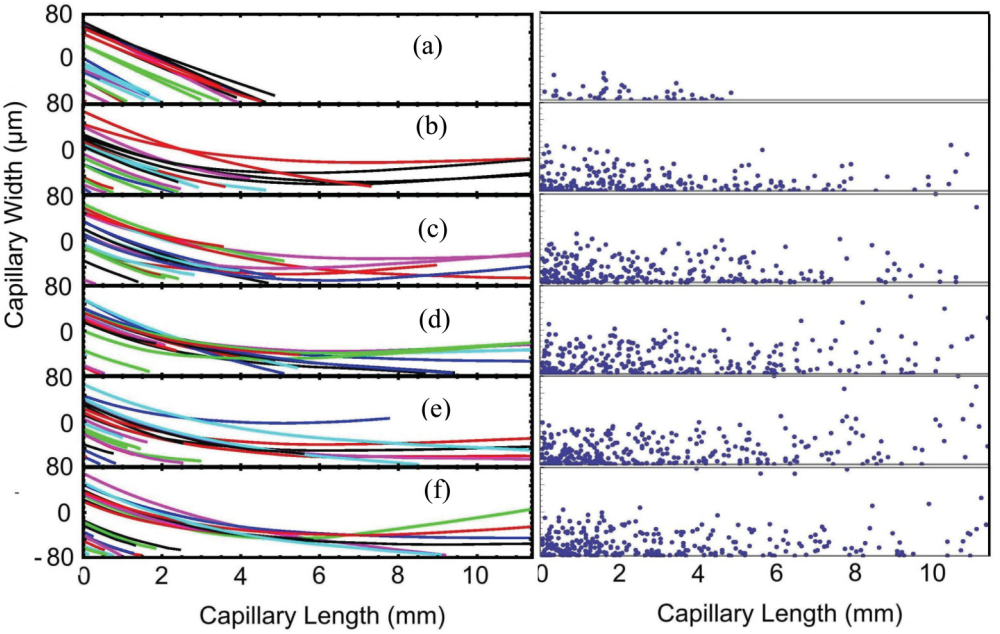

FIG. 3. (Color online) Trajectories of 4.5 keV Ar^{7+} (left-hand panels) and corresponding distributions for the deposited charges (right-hand panels). The titlt angle is 2° and the decay rate for the bulk conductivity is equal to $\Gamma = 10$ mHz. The inserted charge Q_{in} is equal to 0.1 pC in (a), 1.1 pC in (b), 6.8 pC in (c), 13 pC in (d), 21 pC in (e), and 27 pC in (f).

angle. This behavior is plausible from the right-hand panels, which show that no charge patches are created in addition to the entrance patch. The missing charge patches are attributed to the relatively high bulk conductivity, which quickly depletes the deposited charges.

B. Ion transmission and mean emission angle

To obtain more quantitative information about the ions emerging from the capillary exit, the transmitted ion fraction $f = n_t/n_0$ and the mean angle $\overline{\alpha} = n_t^{-1} \sum_i^{n_t} \alpha_i$ were evaluated, where α_i is the emission angle of the ith ion and n_t is the total number of transmitted ions in relation to the total number n_0 of inserted ions. Figure 4 shows three different cases at the decay rates of 10, 0.6, and 0.35 mHz. The quantities f and $\overline{\alpha}$ are plotted in the upper and lower panels, respectively. The results from the previous Figs. 2 and 3 are given in the first two columns, which will be discussed first.

From Figs. 4(a) and 4(b) it is seen that the ion fraction f increases with increasing inserted charge Q_{in} until an equilibrium value is reached. Then the ion fraction remains constant, i.e., ion-blocking effects [37] are not observed. The solid lines in the upper panels represent fits by Eq. (5) assuming that the ion transmission is proportional to the deposited charge.

The equilibrium value for the decay rate of 10 mHz is a factor of 4 smaller than that for 0.6 mHz. This is plausible as in the first case the high charge loss reduces the entrance charge patch so that only a limited part of the incident ions are deflected to the capillary exit. The mean emission angle depicted in the lower panels Figs. 4(d) and 4(e) are in accordance with the results given in Figs. 2 and 3. For the high decay rate of 10 mHz the mean emission angle remains constant, whereas for a low decay rate of 0.6 mHz this angle oscillates with increasing charge insertion.

The results in Figs. 4(c) and 4(f) are obtained with an even smaller decay rate of 0.35 mHz. The transmitted ion fraction exhibits irregular fluctuations jumping up and down in a quasirandom manner, which is somewhat affected by the number of charges deposited per ion on the capillary wall. A similar irregular dependence is observed for the mean emission angle as a function of the charge insertion. These random fluctuations are in agreement with the results obtained by Gruber *et al.* [18] for the capillary cooled to −24 °C. In this case, the conductivity is very low so that the charge patches become overloaded, which limits the regular ion guiding. On the other hand, measurements at the temperature of 44 °C [18], involving a high conductivity, yielded a nearly constant emission angle in good agreement with the present results [Fig. 4(d)].

Next, in Fig. 5 the ion transmission f and mean emission angle $\overline{\alpha}$ are compared for the tilt angles $\psi = 0°, 3°$, and $5°$. The decay rate is equal to 0.6 mHz so that the data shown before in Figs. 4(b) and 4(e) can be included in the comparison. Figure 5(a) indicates that for $\psi = 0°$ the ion transmission at equilibrium is equal to 65%. This limited transmission is due to the divergence of the beam. (The value of 70% follows from the analytic expression given in Ref. [38].) As usual the transmitted ion fraction at equilibrium decreases with increasing tilt angle [Figs. 5(a)–5(c)]. This decrease is governed by the guiding angle which will be discussed in detail below.

The lower panels in Fig. 5 depict the mean emission angle of the transmitted ions. As expected for $\psi = 0°$ this angle is nearly constant without significant deviations from zero. For 3° and 5° the mean emission angle exhibits oscillations

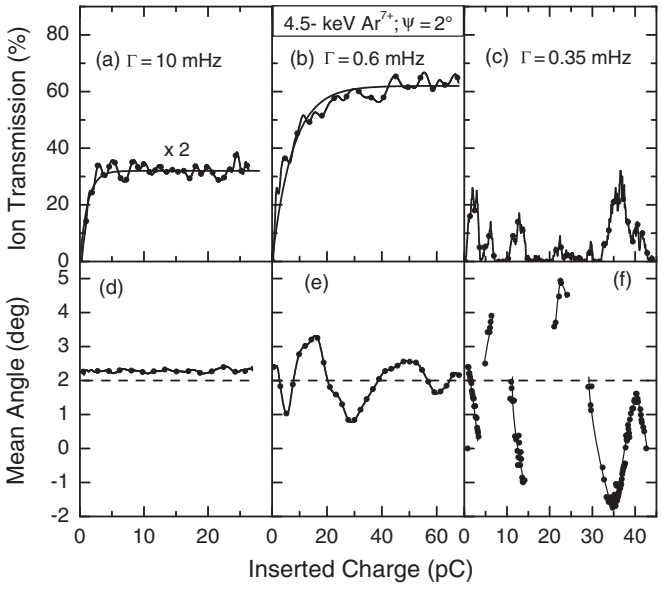

FIG. 4. Transmitted ion fraction f (upper panels) and mean emission angle $\overline{\alpha}$ (lower panels) obtained from the analysis of the trajectories partially shown in Figs. 2 and 3. The tilt angle is 2°. The decay rates are 10, 0.6, and 0.35 mHz as indicated in the panels. The solid lines in the upper panels represent fits to the data using Eq. (5).

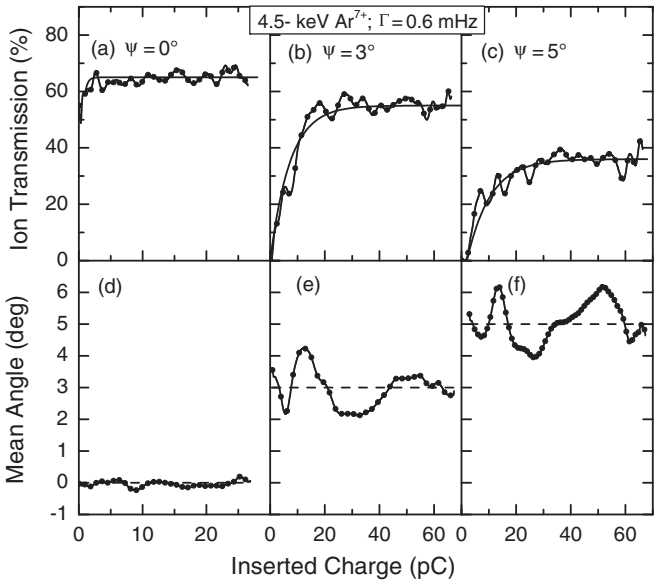

FIG. 5. Transmitted ion fraction f and mean emission angle $\overline{\alpha}$ obtained from the analysis of the trajectories partially shown in Fig. 2. The tilt angles are 0°, 3°, and 5° as indicated in the panels. The charge decay rate is 0.6 mHz. The solid lines in the upper panels represent fits to the data using Eq. (5).

around a value equal to the tilt angle. These oscillations are nearly equal in amplitude and frequency for the three nonzero tilt angles (including the results for 2° in the previous figure). This constancy is somewhat unexpected as the amplitude is supposed to decrease for tilt angles smaller than 2°, as the amplitude is minor for 0°.

C. Potential and field components

To gain more information about the self-organization of the ion guiding, additional electrical quantities are analyzed in the following. Within the capillary, we consider the potential and field components relevant for the cases presented before (Figs. 4 and 5). In Fig. 6 the results for $x = 0$ and three different y values are plotted: for the potential and the field components E_y and E_z the solid line with points, the solid line, and the dashed line represent data for $y = -60$, 0, and 60 μm, respectively. The field E_x refers to $x = -60$, 0, and 60 μm with $y = 0$. The results are plotted along the capillary length (z axis). The inserted charge is equal to 56 pC, which corresponds to equilibrium conditions. Recall that at equilibrium the transient charge patches disappear (Fig. 2). Therefore, only data for the first part up to 2 mm are shown, as the potential and the field components are minor in the other part of the capillary.

In Fig. 6(a) the three potential curves exhibit a maximum near the entrance charge patch. Starting from the capillary entrance, the potentials rise rapidly, producing a field component E_z that reaches the absolute value of 0.1 V/μm [see Fig. 6(d)]. The field E_z cannot contribute to the perpendicular charge migration into the bulk. (Also, as noted already, E_z is too weak for surface migration.) However, E_z may influence the ion trajectories by deceleration and acceleration effects. Moreover, as seen in Fig. 6(b), the field component E_x is quite small. It consists essentially of statistical noise, produced by ion charges randomly distributed over the capillary wall. Since it was not known *a priori* whether it is always negligible, E_x was included in the simulations. Nevertheless, E_x turned out to be small in all calculations so that it will not be further considered.

Looking again at the three potential curves in Fig. 6(a), it is noted that the variation of the potential with respect to the y axis is responsible for the field component E_y. This component, depicted in Fig. 6(c), has a maximum within the entrance charge patch reaching 0.15 V/μm. As expected, E_y is larger at the bottom close to the charge patch than in the upper capillary region. Therefore, the ions incident at different y values undergo different deflection, so that ion focusing effects occur [see Fig. 2(b)]. The focusing can be considered as a general phenomenon that supports the ion guiding.

Next, in Fig. 7 the potential and field components are presented for additional values of the inserted charge Q_{in}. The charge range covers the dynamical period of the guiding process until equilibrium is reached at the higher values of Q_{in} (Fig. 7). It is seen from Fig. 7(a) that the potential remains practically constant when th Q_{in} increases from 17 to 56 pC. The same is true for the field component E_y [Fig. 7(b)]. This charge dependence is consistent with Eq. (5), assuming that the potential V and the field component E_y are proportional to the charge deposited in the entrance patch. Moreover, with increasing Q_{in}, the maxima of V and E_y are shifted closer to the capillary entrance. This shift is due to the increasing ion deflection when the entrance patch is enhanced. Then the ions

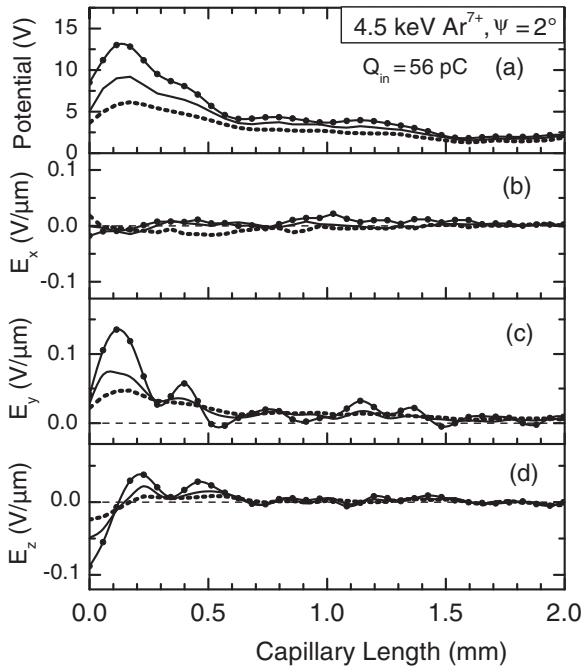

FIG. 6. Potential V and field components E_x, E_y, and E_z. The data were calculated with a charge insertion of $Q_{\text{in}} = 56$ pC. For E_y the solid line with points, the solid line, and the dashed line represent data for $y = -60$, 0, and 60 μm, respectively, where $x = 0$. The field E_x refers to $x = -60$, 0, and 60 μm with $y = 0$.

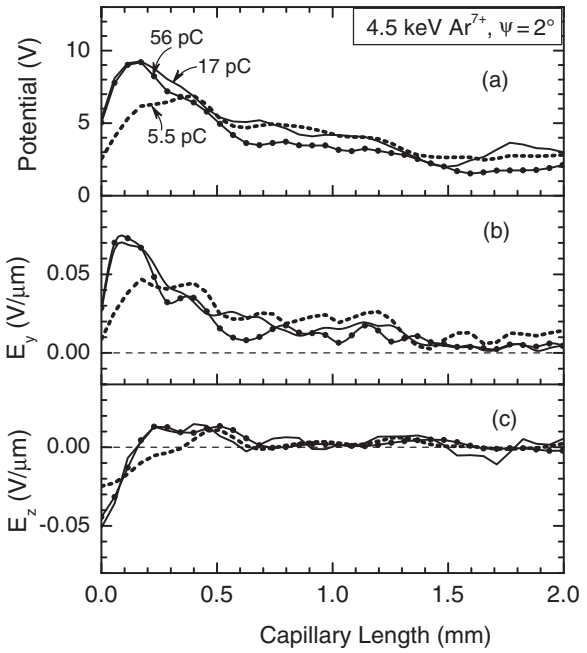

FIG. 7. Potential V and field components E_y and E_z. The data are calculated for a tilt angle of 2°. The dashed line, solid line, and solid line with points represent data for $Q_{\text{in}} = 5.5$, 17, and 56 pC, respectively, where $x = y = 0$.

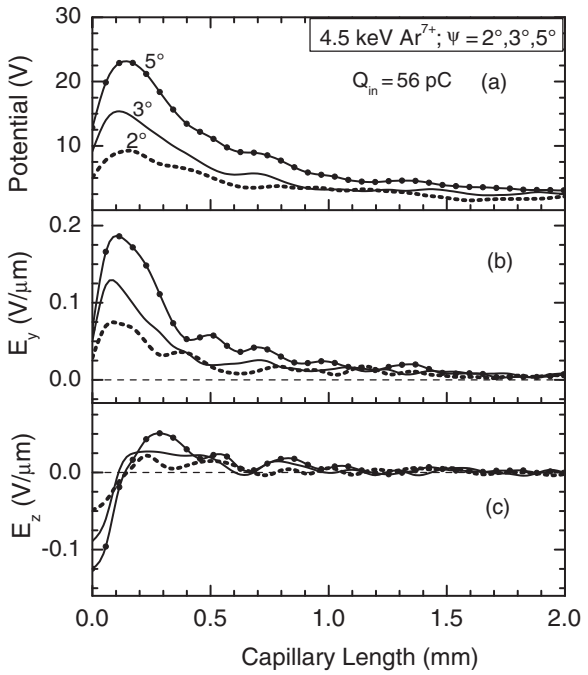

FIG. 8. Potential V and field components E_y and E_z. The data are calculated with the charge insertion of $Q_{\text{in}} = 56$ pC. The dashed line, solid line, and solid line with points represent data for the tilt angles of 2°, 3°, and 5°, respectively, where $x = y = 0$.

hit predominantly the forward part of the charge patch closer to the capillary entrance (Fig. 2).

The major effect of the field component E_y is the deflection of the incident ions towards the capillary exit. As E_y saturates, the ion deflection also saturates with increasing charge insertion (see also Fig. 2). This observation enlightens the self-organizing mechanism that maintains the guiding process at equilibrium. The balance of the charge deposition, the charge migration into the bulk, and the ion deflection produces a well-tailored charge patch that ensures a direct ion transmission from the capillary entrance to the exit.

Finally, the potential V and the field components E_y and E_z are presented for additional tilt angles. Figure 8 shows results for $\psi = 2°$, 3°, and 5° as a dashed line, a solid line, and a solid line with dots, respectively. The data refer to a charge insertion of 56 pC, which ensures equilibrium. Again, within the entrance charge patch the potentials exhibit a maximum, which increases with tilt angle. However, the location of the maximum remains rather constant, i.e., it is not shifted along the capillary axis. Similar results are observed for the field component E_y, i.e., it increases with charge insertion, while the peak location does not move.

In Fig. 8(a) the maximum of the potential V reaches ~25 V, which is still significantly smaller than the 643 V needed to create a potential barrier that cannot be overcome by the 4.5 keV Ar^{7+}ions. The barrier cannot be achieved by increasing the charge insertion as the potential saturates. To reach the barrier one should drastically increase the incident ion current. Likewise, one could decrease the bulk conductivity. However, before the potential barrier is reached the charge patch would become strongly overloaded so that the regular ion guiding would end [as in Figs. 4(c) and 4(f)].

For ion guiding the important effect of the potential V and the field component E_y is the compensation of the perpendicular energy of the incident ions. Looking back at Eq. (1) one may expect that the potential difference U_s increases with $\sin^2\psi$. However, the data in Fig. 8 indicate that V and E_y are proportional to $\sin\psi \approx \psi$. In fact, the application of Eq. (1) is limited due to the finite extension of the entrance patch. The ion deflection stops after the passage of the patch, indicating that its length should be taken into account in a refined analysis. As shown in detail previously [32], the effective "potential" to deflect the incident ions along the capillary axis is given by

$$U_e \approx \overline{E}_y l_e, \tag{8}$$

where $\overline{E}_y$ is averaged over the length l_e of the entrance patch. The ion deflection angle θ is obtained as $\sin\theta = qU_e/2T_p$ so that with $\theta = \psi$ the mean field reads

$$\overline{E}_y = \frac{2T_p}{ql_e}\sin\psi. \tag{9}$$

Indeed, for a constant l_e it follows that $\overline{E}_y$ is proportional to $\sin\psi$ and, likewise, the potential V, in agreement with the simulations (Fig. 8).

It should be added that for nanocapillaries it was found that, surprisingly, the mean field $\overline{E}_y$ remains nearly constant with increasing tilt angle [32]. Instead the length l_e of the charge patch increases linearly with $\sin\psi$, which appears to be counterintuitive. The reason for the unexpected behavior of $\overline{E}_y$ is the stabilization of the field resulting from the nonlinear effects involved in nanocapillaries. Nevertheless, Eq. (8) shows that either $\overline{E}_y$ or l_e can be increased to enhance the potential U_e and, thus, compensate the perpendicular energy.

D. Evaluation of the guiding power

In the following, the transmitted ion fraction at equilibrium is studied as a function of the tilt angle. This is done to determine the guiding angle, which is a measure of the guiding power of the capillary. Before showing the main data, some results for nanocapillaries are presented to reveal differences in comparison with the macrocapillary. It is recalled that for nanocapillaries the surface conduction is dominant. It is governed by the carrier mobility, which is proportional to the surface conductivity [31]. Also, it is recalled that the surface charge transfer is strong affected by a nonlinear field dependence.

In Fig. 9 the transmitted ion fraction is shown for different values of the surface carrier mobility, which is varied by more than one order of magnitude from 0.003 to 0.04 m^2/V s. The results of the simulations are presented as full points. As usual, the transmitted ion fraction is fitted by a Gaussian-like function [18,39]

$$f(\psi) = f_0 \exp\left(-\frac{\sin^2\psi}{\sin^2\psi_c}\right), \tag{10}$$

where $f_0 = f(0)$ and ψ_c is the guiding angle obtained as a fit result. In Fig. 9 the guiding angle is indicated at each curve (solid line) representing the fit by Eq. (10). It should

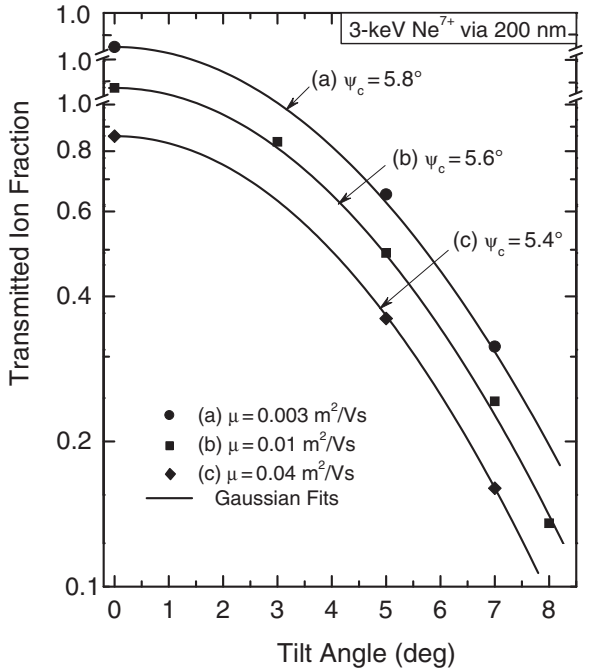

FIG. 9. Fraction of 3 keV Ne^{7+} ions transmitted through PET nanocapillaries with a diameter of 200 nm. The data points are calculated using the carrier mobilities μ indicated in the figure. The solid lines are fits by Eq. (10), yielding the guiding angles ψ_c given at each curve. Most data points are taken from Refs. [31,32].

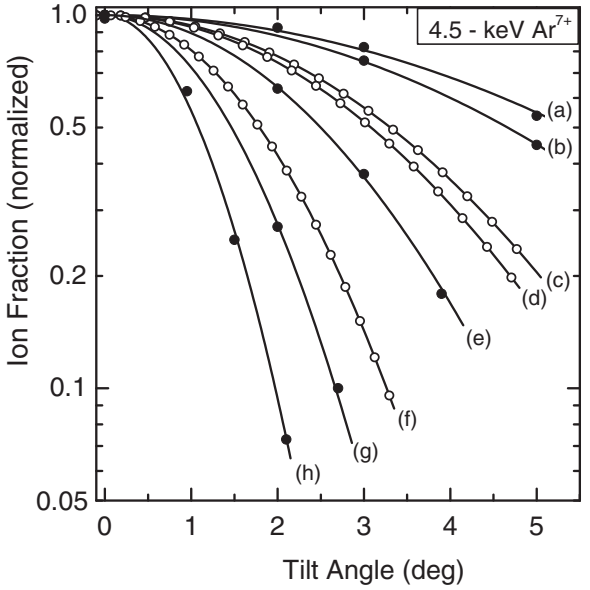

FIG. 10. Transmitted ion fraction as a function of the tilt angle for a variety of decay rates of the deposited charges. The solid points are results from the simulations and the open circles are fit results from experiment [18]. The data are fitted by a Gaussian-like function from Eq. (10). The values for the decay rates and the corresponding guiding power are summarized in Table II.

be noted that most of the nanocapillary data have been taken from previous work by the author. The curve labeled (b) has already been given in [32]. The curves (a) and (c) are generated here from previous data for 5° [31] and data for 7° calculated in the present work. It is noted that the frames of the curves are shifted by a constant value (0.8) to avoid overlap of the curves.

This overlap may happen as the three curves are practically equal. This constancy is a direct result of stabilizing effects originating from the nonlinear formation of the entrance charge patch. Unaffected by the carrier mobility (or the corresponding surface conductivity) the field in the region of the entrance charge patch remains nearly constant. Hence, the propagation of the incident ions through the capillary is essentially independent of the surface conductivity. Figure 9 shows that this is true at least for a region in which the carrier mobility changes by more than a factor of 10. More details are given in the original work [31,32].

Next, the simulations concerning the macrocapillary are treated. In accordance with Gruber *et al.* [18], the equilibrium fraction $f(\psi)$ was normalized by the corresponding value $f_0 = 0.65$ for zero tilt angle. Examples of the equilibrium fraction were given before in Fig. 5 for different tilt angles, including zero degree. As noted, the equilibrium fraction f_0 is smaller than unity due to the divergence of the beam. In Fig. 10 the normalized ion fraction is plotted as a function of the tilt angle for a variety of decay rates Γ.

In the second and third columns of Table II values are given for the decay rates used in the simulations and the corresponding guiding angles. The decay rate was changed by a factor of 25, i.e., the highest curve labeled (a) is obtained with the decay rate of 0.6 mHz and the lowest curve labeled h involves the decay rate of 15 mHz. It is seen that the guiding angle decreases with increasing decay rate. Hence, the guiding power significantly changes with the change of the bulk conductivity.

In Fig. 10 the simulations are compared with the results from the measurements [18]. The experimental data exhibit a significant scatter. For graphical reasons, instead of plotting the scattered values, Fig. 10 shows the results of the corresponding fits by Eq. (10) also performed in previous work [18]. These

TABLE II. Data for the curves labeled (a)–(h) in Fig. 10. The second and third columns give the decay rate (Rate) and the guiding angle (Angle), respectively, used in the simulations. The fourth and the fifth columns give the corresponding temperature (Temp.) of the capillary and the bulk conductivity (Cond.), respectively, from Ref. [18]. The last column contains the decay rate (Rate) obtained from the conductivity using Eq. (4).

Curve (label)	Rate (mHz)	Angle (deg)	Temp.[a] (°C)	Cond.[a] (10^{-16} S/cm)	Rate[a] (mHz)
(a)	0.6	6.45			
(b)	1.5	5.6			
(c)	3.3	4.0	10	1.55	0.62
(d)	3.6	3.7	22	7.3	3.1
(e)	5	3.0			
(f)	8	2.15	44	71	28
(g)	10	1.78			
(h)	15	1.35			

[a]From Ref. [18]

results are depicted as open circles. (For the measured data points the reader is referred to the original work.) Also, simulations were performed to reproduce the experimental results (see the solid lines behind the open circles). The decay rates used in those simulations are also given in the second column of Table II.

The curves with the open circles labeled (c), (d), and (f) were obtained in the experiments by setting the capillary temperature to 10, 22, and 44 °C, respectively (Table II). Also listed in Table II are the specific bulk conductivities [18], which are strongly changing from 1.55×10^{-16} to 71×10^{-16} S/cm. A similar change can be seen in the last column of Table II, which contains the decay rate Γ obtained from the conductivity by means of Eq. (4).

The main feature of the experimental results, i.e., the decrease of the guiding power with increasing conductivity, is qualitatively reproduced by the simulations. It can be attributed to the charge loss in the entrance patch, which limits the deflection of the incident ions so that fewer ions reach the capillary exit. The decay rates used in the simulations can be compared with those derived from the experimental results (second and last columns in Table II). For the label (d), involving the temperature of 22 °C, the decay rates agree quite well. However, the discharge rates for 10 °C (c) and for 44 °C (f) disagree by about factors of 5 and 3.5, respectively. Altogether, the decay rate of the experiment changes more rapidly than that adopted in the simulations. The reason for this discrepancy is not known. It should be noted, however, that the conductivities of insulators involve huge uncertainties so that an agreement within an order of magnitude appears to be acceptable.

Moreover, it is noted that in the experiments the guiding angle reaches a maximum of $\psi_c \approx 4°$. For the temperature of 10 °C, ψ_c increases only by 10% when the capillary is cooled to −10°. In fact, ψ_c does not change any more when the cooling proceeds down to −25° [18], for which a significant decrease of the conductivity is expected (extrapolating the measured curve in [18]). Recall that with decreasing conductivity the guiding becomes irregular and the ion transmission is limited [as in Fig. 4(c)]. Also, nonlinear effects in the bulk conductivity may start to play a role. Recall that the constancy of the guiding angle is a signature for nonlinear charge transport (see Fig. 9).

IV. DISCUSSION AND CONCLUSIONS

Simulations of ion guiding through a macrocapillary were carried out in view of previous experiments [18] wherein the electrical conductivity could be changed in a controlled manner. The calculations were performed using theoretical methods which have previously been applied for nanocapillaries [31,32]. The results of the macrocapillary are also discussed in comparison with previous work performed with nanocapillaries. The essential features of the ion guiding through the macrocapillary were found to be in accordance with the results for nanocapillaries. However, the comparison of the two capillary types exhibits significant differences, which revealed important insights into the self-organization of the guiding process. Indications are found in the simulations that the charge transport within the macrocapillary is essentially governed by a linear conductivity law, whereas for the nanocapillaries nonlinear effects dominate.

For the macrocapillary, the dominant effect depleting the deposited charge is its migration into the bulk material. The fact that the bulk conductivity is dominant is essentially different from situation in nanocapillaries for which the surface conductivity plays the most important role. This difference is primarily caused by the fact that the macrocapillary is orders of magnitude larger than the nanocapillary. In particular, the larger size of the macrocapillary favors the bulk conductivity. One may be tempted to consider a similar scaling of all quantities with the same factor leaving the guiding properties essentially unchanged. However, it should be realized that the bulk and surface conductivities do not follow the same scaling (Table I).

In the case of a high bulk conductivity, the entrance charge patch may directly deflect some of the incident ions to the capillary exit and their emission angle is rather stable. However, in the case of low conductivity the entrance charge patch becomes strong so that the ions may be deflected to the opposite side of the capillary wall. Thus, the ions create additional charge patches, which further deflect the ions. Consequently, the emission angle oscillates as a function of the charge insertion, as similarly observed for nanocapillaries. For an even lower conductivity the charge patches become overloaded and random fluctuations of the ion transmission and the emission angle occur, in agreement with the experiments.

Additional electrical quantities were studied. The potential in the macrocapillary was found to be similar to that in the nanocapillary. However, the corresponding field components are much smaller since the dimensions of the two types of capillaries differ by several orders of magnitude. The potential and the vertical field component increase linearly with the tilt angle. This finding is in disagreement with the nanocapillaries for which the vertical field remains constant. The field difference is attributed to the finding that the macrocapillary and the nanocapillary are dominated by linear and nonlinear effects, respectively. The nonlinear (exponential) increase of the conductivity tends to stabilize the field within the nanocapillary [31,32]. To compensate the vertical energy of the incident ions, the entrance charge patch is extended into the nanocapillary, whereas for the macrocapillary this patch is essentially constant in length. In fact, for both types of capillaries, the length of the entrance charge patch is quite different from the geometric length produced by undeflected ions.

Guiding angles were derived from of the tilt angle dependence of the transmitted ion fraction. In qualitative agreement with the experiment, the simulations show that the guiding angle, and thus the guiding power, decrease with increasing decay rate of the deposited charges. Also, in agreement with experiment, it follows that the guiding angle increases with increasing ion current. The formalism of the simulations provide clear evidence that the variation of the conductivity and the ion current has the same effect on the guiding power. The same conclusion has previously been drawn for nanocapillaries.

However, the dependence on the beam current is completely different from results obtained for nanocapillaries.

Experimentally, it has been found that the equilibrium transmission through nanocapillaries exhibits only minor changes when the incident current is varied within two orders of magnitude [8]. Moreover, in this work additional simulations with nanocapillaries show that the guiding power does not change when the charge carrier mobility was varied by an order of magnitude. The constancy of the ion transmission with varying conductivity or ion current is associated with nonlinear effects limiting the charge deposition in the entrance patch. In fact, one may conclude that the observation of a constant guiding power provides evidence for nonlinear conductivity effects. Thus, it is possible that the near-constancy of the guiding angle experimentally observed for temperatures between 10 and $-24\,^{\circ}$C may be due to the beginning of nonlinear effects of the bulk conductivity.

Discrepancies between the experimental analysis and the simulations were noted. Considering the dependence of the guiding angle, the experimental decay rate was found to vary more rapidly than that of the simulations. For a temperature of $22\,^{\circ}$C the decay rates are in good agreement, whereas for 44 and $10\,^{\circ}$C they disagree by factors between 3 and 5. The reason for this discrepancy is not understood at present. In any case, the conductivity of insulators, which involves large uncertainties, is a complex issue that requires further detailed investigations.

ACKNOWLEDGMENTS

Many thanks are devoted to Fritz Aumayr and Elisabeth Gruber for motivating this study and for detailed information about their experiments. I am indebted to Christoph Lemell, Grigori Pokhil, Yasu Yamazaki, and Bela Sulik for several clarifying discussions. Comments on the manuscript by John Tanis are gratefully acknowledged.

[1] C. Lemell, J. Burgdörfer, and F. Aumayr, Prog. Surf. Sci. **88**, 237 (2013).
[2] N. Stolterfoht, J. H. Bremer, V. Hoffmann, R. Hellhammer, D. Fink, A. Petrov, and B. Sulik, Phys. Rev. Lett. **88**, 133201 (2002).
[3] N. Stolterfoht, V. Hoffmann, R. Hellhammer, D. Fink, A. Petrov, Z. D. Pešić, and B. Sulik, Nucl. Instrum. Methods Phys. Res., Sect. B **203**, 246 (2003).
[4] N. Stolterfoht, R. Hellhammer, Z. D. Pešić, V. Hoffmann, J. Bundesmann, A. Petrov, D. Fink, and B. Sulik, Vacuum **73**, 31 (2004).
[5] G. Víkor, R. R. Kumar, Z. Pešić, N. Stolterfoht, and R. Schuch, Nucl. Instrum. Methods Phys. Res., Sect. B **233**, 218 (2005).
[6] M. B. Sahana, P. Skog, G. Vikor, R. T. Rajendra Kumar, and R. Schuch, Phys. Rev. A **73**, 040901(R) (2006).
[7] S. Mátéfi-Tempfli, M. Mátéfi-Tempfli, L. Piraux, Z. Juhász, S. Biri, É. Fekete, I. Iván, F. Gáll, B. Sulik, G. Víkor *et al.*, Nanotechnology **17**, 3915 (2006).
[8] N. Stolterfoht, R. Hellhammer, J. Bundesmann, D. Fink, Y. Kanai, M. Hoshino, T. Kambara, T. Ikeda, and Y. Yamazaki, Phys. Rev. A **76**, 022712 (2007).
[9] P. Skog, I. L. Soroka, A. Johansson, and R. Schuch, Nucl. Instrum. Methods Phys. Res., Sect. B **258**, 145 (2007).
[10] Y. Kanai, M. Hoshino, T. Kambara, T. Ikeda, R. Hellhammer, N. Stolterfoht, and Y. Yamazaki, Nucl. Instrum. Methods Phys. Res., Sect. B **258**, 155 (2007).
[11] Y. F. Chen, X. M. Chen, F. J. Lou, J. Z. Zhang, J. X. Shao, G. Z. Sun, J. Wang, F. Y. Xi, Y. Z. Yin, X. A. Wang *et al.*, Chin. Phys. B **18**, 2739 (2009).
[12] N. Stolterfoht, R. Hellhammer, Z. Juhász, B. Sulik, V. Bayer, C. Trautmann, E. Bodewits, A. J. de Nijs, H. M. Dang, and R. Hoekstra, Phys. Rev. A **79**, 042902 (2009).
[13] M. Kreller, G. Zschornak, and U. Kentsch, J. Phys.: Conf. Ser. **163**, 012090 (2009).
[14] R. Bereczky, G. Kowarik, F. Aumayr, and K. Tökési, Nucl. Instrum. Methods Phys. Res., Sect. B **267**, 317 (2009).
[15] R. Bereczky, G. Kowarik, C. Lemaignan, A. Mace, F. Ladinig, R. Raab, F. Aumayr, and K. Tökési, in *Application of Accelerators in Research and Industry: 21st International Conference*, edited by F. D. McDaniel and B. L. Doyle, AIP Conf. Proc. Vol. 1336 (AIP, New York, 2011), p. 119.
[16] G. Kowarik, R. J. Bereczky, F. Aumayr, and K. Tökési, Nucl. Instrum. Methods Phys. Res., Sect. B **267**, 2277 (2009).
[17] R. Nakayama, M. Tona, N. Nakamura, H. Watanabe, N. Yoshiyasu, C. Yamada, A. Yamazaki, S. Ohtani, and M. Sakurai, Nucl. Instrum. Methods Phys. Res., Sect. B **267**, 2381 (2009).
[18] E. Gruber, G. Kowarik, F. Ladening, J. P. Waclawek, F. Aumayr, R. J. Bereczky, K. Tökési, P. Gunacker, T. Schweigler, C. Lemell *et al.*, Phys. Rev. A **86**, 062901 (2012).
[19] T. Ikeda, Y. Kanai, T. M. Kojima, Y. Iwai, T. Kambara, Y. Yamazaki, M. Hoshino, T. Nebiki, and T. Narusawa, Appl. Phys. Lett. **89**, 163502 (2006).
[20] T. Ikeda, T. M. Kojima, Y. Iwai, Y. Kanai, T. Kambara, T. Nebiki, T. Narusawa, and Y. Yamazaki, J. Phys.: Conf. Ser. **58**, 68 (2007).
[21] A. Cassimi, T. Muranaka, L. Maunoury, H. Lebius, B. Manil, B. A. Huber, T. Ikeda, Y. Kanai, T. M. Kojima, Y. Iwai *et al.*, Int. J. Nanotechnol. **5**, 809 (2008).
[22] M. Kreller, G. Zschornak, and U. Kentsch, Nucl. Instrum. Methods Phys. Res., Sect. B **269**, 1032 (2011).
[23] G. P. Pokhil, K. A. Vokhmyanina, L. A. Zhilyakov, and T. I. Y. Yamazaki, Bull. Russ. Acad. Sci.: Phys. **74**, 221 (2010).
[24] G. P. Pokhil and V. V. Cherdyntsev, J. Surf. Investigation: X-ray, Synchrotron Neutron Techniques **7**, 356 (2013).
[25] Y. Iwai, T. Ikeda, T. Kojima, Y. Yamazaki, K. Maeshima, N. Imamoto, T. Kobayashi, T. Nebiki, T. Narusawa, and G. P. Pokhil, Appl. Phys. Lett. **92**, 023509 (2008).
[26] K. Schiessl, W. Palfinger, C. Lemell, and J. Burgdörfer, Nucl. Instrum. Methods Phys. Res., Sect. B **232**, 228 (2005).
[27] K. Schiessl, W. Palfinger, K. Tökési, H. Nowotny, C. Lemell, and J. Burgdörfer, Phys. Rev. A **72**, 062902 (2005).
[28] K. Schiessl, W. Palfinger, K. Tökési, H. Nowotny, C. Lemell, and J. Burgdörfer, Nucl. Instrum. Methods Phys. Res., Sect. B **258**, 150 (2007).
[29] K. Schiessl, C. Lemell, K. Tökési, and J. Burgdörfer, J. Phys.: Conf. Ser. **163**, 012081 (2009).

[30] T. Schweigler, C. Lemell, and J. Burgdorfer, Nucl. Instrum. Methods Phys. Res., Sect. B **269**, 1253 (2011).
[31] N. Stolterfoht, Phys. Rev. A **87**, 012902 (2013).
[32] N. Stolterfoht, Phys. Rev. A **87**, 032901 (2013).
[33] J. Frenkel, Phys. Rev. **54**, 647 (1938).
[34] Borosilicate glass (Duran) from www.duran-group.com.
[35] R. T. Rajendra-Kumar, X. Badel, G. Vikor, J. Linnros, and R. Schuch, Nanotechnology **16**, 1 (2005).
[36] Data sheets for PET (Mylar) from DuPont Teijin Films www.dupontteijinfilms.com.
[37] N. Stolterfoht, R. Hellhammer, B. Sulik, Z. Juhász, V. Bayer, C. Trautmann, E. Bodewits, and R. Hoekstra, Phys. Rev. A **83**, 062901 (2011).
[38] N. Stolterfoht, R. Hellhammer, B. Sulik, Z. Juhász, V. Bayer, C. Trautmann, E. Bodewits, G. Reitsma, and R. Hoekstra, Phys. Rev. A **88**, 032902 (2013).
[39] N. Stolterfoht, R. Hellhammer, D. Fink, B. Sulik, Z. Juhász, E. Bodewits, H. M. Dang, and R. Hoekstra, Phys. Rev. A **79**, 022901 (2009).